JOURNAL OF Materials CHEMISTRY

Stoichiometry and defect structure of '$NdMnO_3$'

Elaine T. Maguire, Alison M. Coats, Janet M. S. Skakle and Anthony R. West

University of Aberdeen, Department of Chemistry, Meston Walk, Aberdeen, Scotland, UK AB24 3UE

Received 27th January 1999, Accepted 17th March 1999

The phase '$NdMnO_3$' has been synthesised and characterised by a combination of electron probe microanalysis, X-ray and neutron diffraction and H_2-reduction thermogravimetry. $NdMnO_3$ forms, at $\approx$1400 °C, over the range $Nd_{1.00(1)}Mn_{0.95(1)}O_{2.92(1)}$ to $Nd_{0.88(1)}Mn_{1.00(1)}O_{2.72(1)}$. Oxygen contents vary in air over the range 700 to 1400 °C and can be varied further, either by high pressure O_2 treatment or by reduction in H_2. The structure of '$NdMnO_3$' is based on the $GdFeO_3$ structure with a Jahn–Teller distortion associated with the high proportion of Mn^{3+} ions present. However, it also shows a very varied defect structure; depending on composition and heat treatment, vacancies can form on any one or any two of the three sublattices, Nd, Mn and O and the overall Mn oxidation state can include 2+, 3+ and 4+ contributions. Data on compositional range and defect crystal structure are presented in the form of a novel phase diagram–defect structure map.

Introduction

Rare earth manganites have been studied because of interest in their electrical, catalytic and mechanical properties.[1,2] They are used as electrodes in solid oxide fuel cells and are the parent compounds of colossal magnetoresistors. The discovery of the colossal magnetoresistance (CMR) effect in rare earth manganites has resulted in many studies on these systems. CMR has been observed in at least three families of manganese oxides: the perovskites (general formula $A_{1-x}A'_xMnO_3$, A = La, Pr, Y…; A′ = Ca, Sr, Ba…),[3–18] the Ruddlesden–Popper (RP) phases (general formula $(A_{1-x}A_{x}')_{n+1}Mn_nO_{3n+1}$[19–27] and the $Tl_2Mn_2O_7$ pyrochlore.[28]

The rare earth manganite $NdMnO_3$ belongs to the group of orthorhombically-distorted perovskites $RMnO_3$, where R is a rare earth ion from La^{3+} to Dy^{3+}, with the $GdFeO_3$ structure. It is, however, a much more complex material than indicated by this simple composition, because both the Nd : Mn ratio and the oxygen content appear to be variable. Studies of rare earth manganites have centred on the La–Mn–O system and to a lesser extent, the Nd–Mn–O system. Various authors have studied the oxygen nonstoichiometry of $LaMnO_3$ and its effect on the crystal structure.[29–33] Depending on temperature and oxygen partial pressure, '$LaMnO_3$' exhibits either an oxygen excess or oxygen-deficiency and, depending on the oxygen content, different polymorphs form; for $LaMnO_{3+\delta}$, $0 \leqslant \delta < 0.10$, the structure is orthorhombic $GdFeO_3$-type, whilst for $0.10 \leqslant \delta < 0.3$ it is rhombohedral $LaAlO_3$-type.[34–38]

The defect structure of such 'oxygen excess' phases is described by cation vacancies on the metal sublattices.[29–33] The analogous '$NdMnO_3$' system is expected to behave similarly. Cherepanov *et al.*[39] reported 'oxygen excess' $NdMnO_{3+\delta}$: in air, the maximum δ, $NdMnO_{3.071}$, was obtained at 1100 °C and the lowest, $NdMnO_{3.01}$, at 1500 °C, whereas at 1100 °C in air Atsumi *et al.*[40] reported the stoichiometry to be $NdMnO_{2.97}$. Similarly to $LaMnO_{3+\delta}$, the defect structure of $NdMnO_{3+\delta}$ is described by cation vacancies.[39]

As part of a larger study on the '$RMnO_3$' oxides (R = La, Pr, Nd) to resolve discrepancies in the literature and establish cation and oxygen stoichiometry ranges, a detailed study of '$NdMnO_3$' has been made. The problems of characterising variable R : Mn ratios and oxygen contents have been addressed using a combination of techniques: electron probe microanalysis (EPMA) to determine cation ratios, thermogravimetry (TG) to determine absolute oxygen contents and X-ray diffraction (XRD) and neutron diffraction (ND) to determine possible defect structures.

Experimental

Samples along the $NdO_{1.5}$–MnO_2 pseudobinary join were prepared by standard solid state techniques. Appropriate proportions of the starting materials, Nd_2O_3 (Aldrich 99.9%, dried at 1000 °C before use) and MnO_2 (Aldrich 99+%), were mixed with acetone using an agate mortar, dried, pelleted (13 mm diameter, pressed under 2 tonnes per square inch), reacted in Pt boats at 1400 °C for 72 h and subsequently annealed, either in air at various temperatures in the range 600–1200 °C for 2 h, or under high oxygen pressures at 700 °C for 16 h using a Morris Research Inc. high oxygen pressure furnace, Model No. HP5015E7. For the latter, a starting pressure of $\approx$70 bar at room temperature was used which increased to $\approx$200 bar at 700 °C. At the end of the heat treatment samples were cooled slowly (1 °C min^{-1}) to room temperature whilst still under pressure.

XRD was performed with a Stoe Stadi P diffractometer using a small linear position sensitive detector of resolution 0.02° 2θ with Cu-Kα_1 radiation and an external Si standard. Unit cell parameters were refined using Stoe proprietary software (LATREF). For ND, $\approx$10 g samples were prepared and placed in cylindrical V cans. Data were collected on the POLARIS diffractometer at ISIS, Rutherford Appleton Laboratory, over the time-of-flight range 2000–19530 μs. Structural models were refined using TF14LS from the Cambridge Crystallography Subroutine Library.[41,42] Scattering lengths were taken from Sears.[43]

Samples were analyzed by EPMA using a Cameca SX51 fitted with four wavelength-dispersive spectrometers. Pellets sintered at either 1400 °C, 72 h or 1500 °C, 72 h, were set in epoxy resin, polished to $<$1 μm surface roughness and carbon-coated prior to analysis. Quantitative analysis was performed to determine the number and distribution of phases present and where appropriate, the composition of each phase. The concentrations (wt%) of Nd and Mn were determined with a fixed beam of 20 kV and 30 nA at 10 different points on the sample surface. A single crystal of $NdGaO_3$ (National Crystal Growth Facility, Oxford) was used as the standard for Nd and $MnSiO_3$, Rhodonite (Micro-Analysis Consultants), for Mn. Element maps (qualitative analysis) were also obtained for representative samples. Oxygen contents were not determined directly by EPMA but were estimated by difference:

$$\text{wt\% O} = 100 - (\text{wt\% Nd} + \text{wt\% Mn})$$

Absolute oxygen contents were determined by hydrogen-

reduction TG, using a Stanton Redcroft TG-DTA simultaneous thermal analyzer STA 1000/1500. Samples ($\approx$0.1 g) were heated in flowing H_2/N_2 (10:90) at 10 °C min^{-1} to 975 °C, which was well above the minimum temperature necessary to achieve constant weight; final reduction products were a mixture of Nd_2O_3 and MnO.

Results and discussion

1 Solid solution limits and sample homogeneity: EPMA analyses

To investigate the possibility that '$NdMnO_3$' forms with a variable Nd:Mn ratio, nominal compositions ranging from $NdMn_{0.25}O_z$ to $Nd_{0.25}MnO_z$ were studied by XRD and EPMA. XRD on samples fired in air at 1400 °C indicated that single phase '$NdMnO_3$' appeared to exist over a small range of compositions from about $NdMn_{0.89}O_z$ to $Nd_{0.82}MnO_z$. Increasing or decreasing the Mn concentration caused Mn_3O_4 or Nd_2O_3 respectively, to be present as a second phase. XRD patterns of single phase solid solution samples, prepared at 1400 °C, 72 h, resembled the powder diffraction file for $NdMnO_3$ (no. 25–0565)[44] and were indexed on an orthorhombic unit cell similar to that of $GdFeO_3$.[32] The variation of the unit cell parameters and unit cell volume with Mn concentration are shown in Fig. 1; b and c remain roughly constant whereas a and V decrease. The unit cell dimensions conform

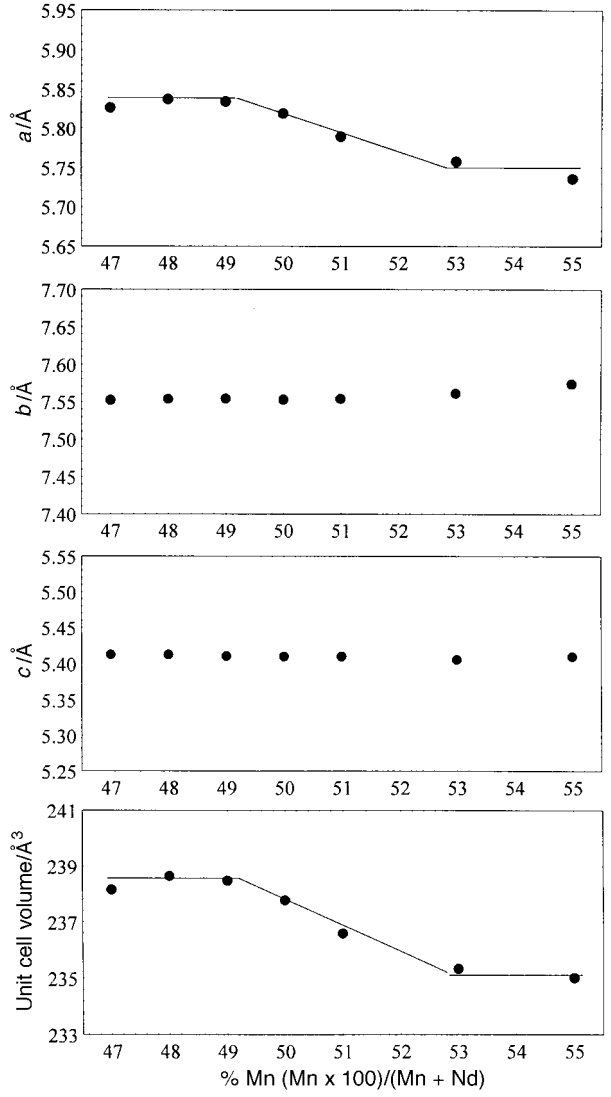

Fig. 1 Variation of the unit cell parameters with composition for as-fired samples.

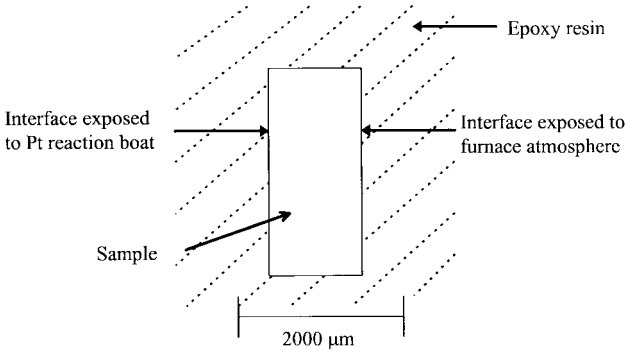

Fig. 2 Schematic of the fracture surface of a pellet of $NdMn_{0.97}O_z$ for analysis by EPMA.

to Goodenough's[45] definition of the O′ orthorhombic structure where $b/c<\sqrt{2}$, $c<a$. This suggests that the structure is $GdFeO_3$-type with a superposed Jahn–Teller (JT) distortion. From the variation of a and V with composition, it appears that a '$NdMnO_3$' solid solution forms from $\approx$49 to $\approx$53 cation% Mn, *i.e.* from $NdMn_{0.95}O_z$ to $Nd_{0.88}MnO_z$. Note that the data in Fig. 1 are for as-fired samples without, at this stage, any attempt to control or determine oxygen contents.

As a first step to confirm the existence of the '$NdMnO_3$' solid solution, it was necessary to determine whether the reaction conditions used had been appropriate to achieve complete reaction without loss of either component or contamination from the sample container. To achieve this, EPMA of fracture surfaces of pellets with starting composition $NdMn_{0.97}O_z$ was carried out. Two pellets which had been heated at 1400 °C, 72 h and 1500 °C, 72 h, respectively were analysed. For each, 20 points located inside grains rather than at grain boundaries were analysed (grain sizes were between 30–40 μm); the points were taken from a band scan (width $\approx$20 μm) across the polished fracture surface, extending from the pellet surface that had been in contact with the Pt container to the surface that had been exposed to the air (Fig. 2). Results are shown in Fig. 3; point 0 corresponds to the Pt interface, point 20 to the air interface.

The average cation stoichiometry, calculated by dividing the determined wt% of each cation by its atomic weight and normalizing with respect to Nd, was $Nd_{1.00(1)}Mn_{0.97(1)}O_z$ which agrees with the nominal composition. In addition, the Nd and Mn contents were constant within errors across the fracture surface for both samples [Fig. 3(a) and (b)]. There was, therefore, no evidence of any concentration gradient of Nd or Mn through the bulk sample and the elemental composition at both interfaces of the pellet (that exposed to the furnace atmosphere and the other to the Pt reaction boat) was similar to that of the bulk sample. There was also no evidence of diffusion of Pt into the sample. A false colour element map of a different solid solution member, $Nd_{0.95(1)}Mn_{1.00(1)}O_z$ (Fig. 4), indicates further the even distribution of Nd, Mn and O throughout the perovskite phase; dark regions are porosity. A backscattered electron image of the same sample was also uniform throughout, again indicating its single phase nature.

The conclusion from these experiments is therefore that the reaction conditions used yielded homogeneous, fully reacted samples with no evidence of loss of reagents or Pt attack. This was found at both 1400 and 1500 °C; consequently even though most samples were prepared at 1400 °C, possible problems of volatilisation and/or contamination would not occur until at least 1500 °C.

Results from quantitative EPMA of several pellets of different nominal compositions are given in Table 1. Since oxygen contents were not determined directly by EPMA, and it is well known that materials such as '$NdMnO_3$' can have variable oxygen contents depending on their thermal history,

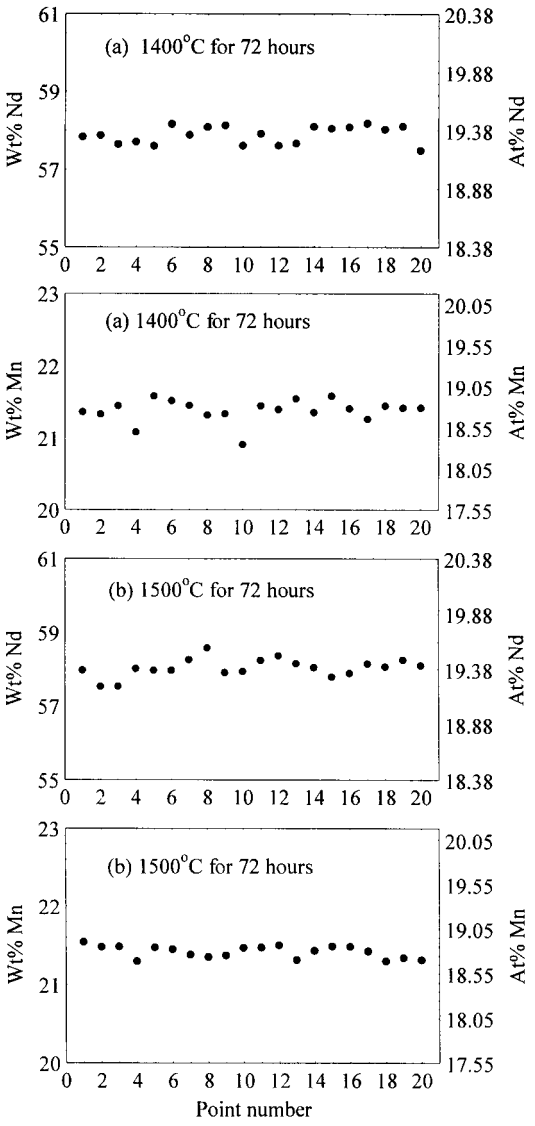

Fig. 3 Quantitative EPMA of pellets of $NdMn_{0.97}O_z$ that had been heated at (a) 1400 °C for 72 h, (b) 1500 °C for 72 h.

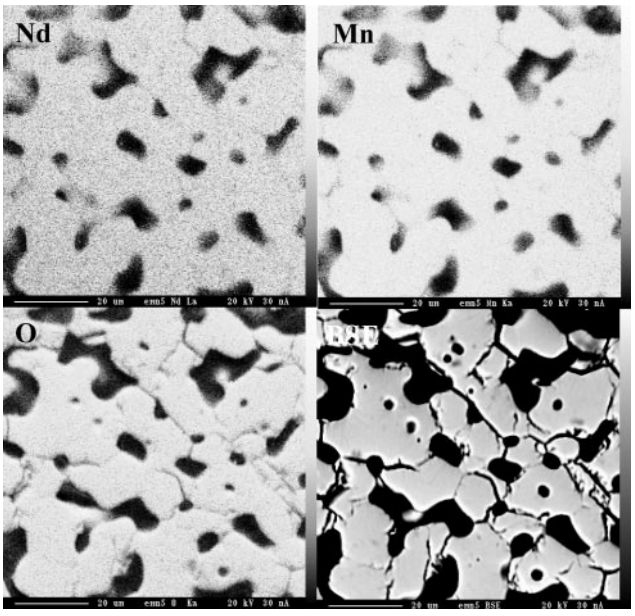

Fig. 4 Element map of $Nd_{0.95(1)}Mn_{1.00(1)}O_z$.

initial focus is on the Nd : Mn ratios; oxygen contents are given nominally as 3 in Table 1. The Nd : Mn contents are scaled such that the higher of the two equals 1 since it is unlikely that interstitial cations can be accommodated in the perovskite structure.

The data in Table 1 show the compositions used in initial syntheses (column 1), the derived atom% contents expected for Nd and Mn assuming 60 at% O (columns 2, 3), the Nd, Mn contents determined by EPMA (columns 4, 5: absolute values, uncorrected), the derived stoichiometry of the perovskite phase assuming oxygen content 3 and scaling Nd and/or Mn contents to 1 (column 6) and the expected and analysed Mn contents as a percentage of the total cation content (columns 7, 8). The Mn contents are also shown graphically in Fig. 5 and demonstrate clearly that a solid solution forms to either side of the '$NdMnO_3$' stoichiometry, although it is most extensive on the Mn-rich side. The solid solution limits may be represented as $Nd_{1.00(1)}Mn_{0.95(1)}O_z$ (49 cation% Mn) and $Nd_{0.88(1)}Mn_{1.00(1)}O_z$ (53 cation% Mn). At higher or lower Mn contents Mn_3O_4 and Nd_2O_3, respectively, were present as second phases (Table 1). Hence, the EPMA results confirm those obtained by XRD in showing the existence of a solid solution. The solid solution limits are comparable to those estimated from the lattice parameters (Fig. 1) but less than those estimated by using apparent phase purity by XRD as a true test of phase purity. This latter discrepancy is readily attributable to the difficulty of detecting small amounts of second phase by XRD; identification of small amounts of Mn_3O_4 is particularly difficult as Mn fluoresces, thus reducing the intensity of the diffraction lines whilst increasing that of the background radiation.

The results in Fig. 5 show not only the compositional extent of the perovskite solid solution but also confirm that for single phase samples the product compositions are essentially the same as those of the starting compositions. These results demonstrate the accuracy of EPMA for the determination of cation ratios; experimental and expected Mn contents agree to within $\pm 0.5\%$ in Fig. 5, *i.e.* to within 1% of the Mn content. However, the results in Table 1 are influenced by unquantified systematic error which reduces the analysed Nd, Mn contents and although the Nd : Mn ratios are as expected, the absolute cation contents (Table 1, columns 4, 5) are systematically less than expected by 1–2% (Table 1, columns 2, 3). In Fig. 6, the differences between expected and analysed cation contents are shown. All analysed values are lower than expected; on average Mn contents are low by 0.95 at% and Nd contents low by 0.55 at%. There is, however, considerable variation, but both Mn and Nd analyses tend to show the same pattern of variation.

The origin of this discrepancy between expected and analysed cation contents is not fully understood; possibilities include the presence of surface imperfections or roughness in the analyzed regions or absorbed water on the sample surface. An additional discrepancy must arise in situations where the oxygen content is variable and not equal to three; as shown later, the oxygen content rarely equals 3 for the present materials and is usually less than 3. Since the Nd, Mn contents are normalised to a maximum of one of each per perovskite ABO_3 subcell, the discrepancies shown in Fig. 6 are an underestimate of the expected values if the true oxygen contents are less than 3. Given the discrepancies between expected and analysed cation contents for the present materials, it is difficult to give absolute values whereas the cation ratios have a much higher accuracy. Effectively therefore, one cation may be used as an internal standard for the determination of the other cation.

It is possible to determine oxygen contents by EPMA, either by direct measurement against a standard or by difference. However, light element analysis has higher intrinsic errors and so direct oxygen analysis was not attempted. Since the absolute

Table 1 Expected composition and analysed atom% of Nd and Mn for samples along the $NdO_{1.5}$–$MnO_{1.33}$ pseudobinary join

	Expected At%[b]		Analysed At%			%Mn cation[c]	
Nominal composition[a]	Nd	Mn	Nd	Mn	Analysed composition[a]	Nominal	Analysed
$NdMn_{0.89}O_3$	21.2	18.8	19.5(2)	18.6(1)	$Nd_{1.00(1)}Mn_{0.96(1)}O_3 + Nd_{2.0(1)}O_{3.4(1)}$[d]	47	49(1)
$NdMn_{0.92}O_3$	20.8	19.2	19.7(1)	18.7(1)	$Nd_{1.00(1)}Mn_{0.95(1)}O_3 + Nd_{2.0(1)}O_{3.4(1)}$[d]	48	49(1)
$NdMn_{0.96}O_3$	20.4	19.6	19.7(2)	18.6(1)	$Nd_{1.00(1)}Mn_{0.95(1)}O_3$	49	48(1)
$NdMnO_3$	20	20	19.3(1)	19.2(2)	$Nd_{1.00(1)}Mn_{1.00(1)}O_3$	50	50(1)
$Nd_{0.96}MnO_3$	19.6	20.4	19.1(2)	19.5(2)	$Nd_{0.98(1)}Mn_{1.00(1)}O_3$	51	51(1)
$Nd_{0.89}MnO_3$	18.8	21.2	18.3(2)	20.0(1)	$Nd_{0.91(1)}Mn_{1.00(1)}O_3$	53	52(1)
$Nd_{0.86}MnO_3$	18.5	21.5	18.1(1)	20.6(1)	$Nd_{0.88(1)}Mn_{1.00(1)}O_3$	54	53(1)
$Nd_{0.82}MnO_3$	18.1	21.9	18.1(2)	20.6(1)	$Nd_{0.88(1)}Mn_{1.00(1)}O_3 + Mn_{3.0(1)}O_{4.1(1)}$[e]	55	53(1)
$Nd_{0.67}MnO_3$	16.0	24.0	18.2(1)	20.6(1)	$Nd_{0.88(1)}Mn_{1.00(1)}O_3 + Mn_{3.0(1)}O_{4.1(1)}$[e]	60	53(1)

[a]Cation contents scaled so that either Mn or Nd or both is unity. Nominal oxygen content of 3. [b]Assuming 60 at% oxygen. [c]%Mn = Mn/(Mn + Nd) × 100. [d]From the Nd content and the absence of Mn, these second phase particles are identified as Nd_2O_3. [e]From the Mn content and the absence of Nd, these second phase particles are identified as Mn_3O_4.

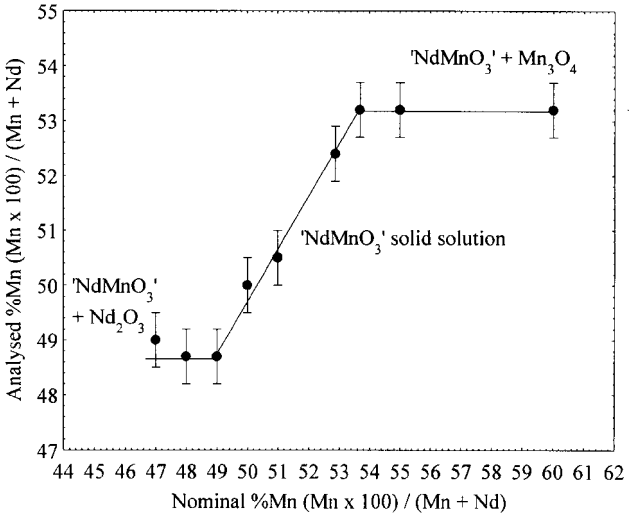

Fig. 5 Analysed Mn% as a function of nominal composition as determined by EPMA for $NdO_{1.5}$–$MnO_{1.33}$ pseudobinary join.

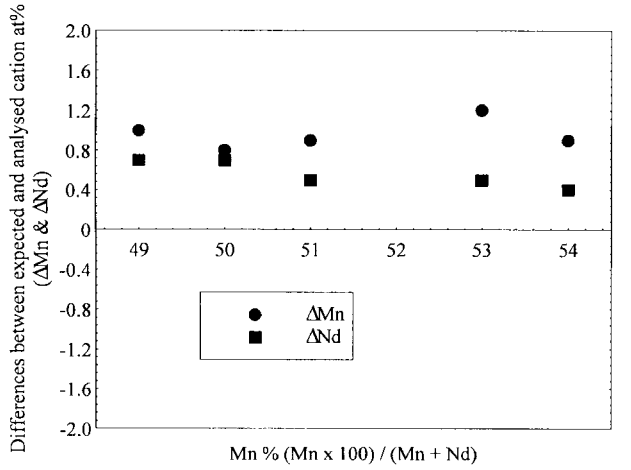

Fig. 6 The difference between the expected and analysed cation contents as a function of Mn content.

cation contents are anomalously low by 1–2%, oxygen analysis by difference leads to an overestimate of the oxygen content by 0.25 to 0.30 per ABO_3 perovskite subcell. Instead oxygen contents were determined by H_2-reduction TG.

2 Oxygen content of '$NdMnO_z$'

The oxygen content, z, of solid solution samples was determined using TG analysis by direct reduction (in flowing H_2/N_2) according to the reaction:

$$NdMnO_z \rightarrow 0.5Nd_2O_3(s) + MnO(s) + (z–2.5)\ H_2O(g) \quad (1)$$

XRD confirmed the presence of Nd_2O_3 and MnO after reduction. Typically, decomposition began at ≈500 °C and was completed by ≈900 °C. The reduction of one composition, $Nd_{1.00(1)}Mn_{0.97(1)}O_z$, prepared at 1400 °C, 72 h, is shown in Fig. 7. Calculation of the oxygen content was based on eqn. (1) where the starting weight of '$NdMnO_z$' was known and the total weight loss was attributed to $H_2O_{(g)}$ loss. Any oxygen nonstoichiometry of MnO, due to the possible mixed valence states of Mn, would result in errors in the oxygen content calculation. However, reduction by TG of the starting material MnO_2 and subsequent XRD analysis indicated that the reduction product, MnO, was stable at the temperatures required for eqn. (1) and that the overall weight loss was as expected for reduction of MnO_2 to MnO. For the data shown in Fig. 7, the oxygen content z was calculated to be 2.92(1).

The oxygen contents of as-prepared solid solution samples, $Nd_{1.00(1)}Mn_{0.95(1)}O_z$ to $Nd_{0.88(1)}Mn_{1.00(1)}O_z$, heated at 1400 °C, 72 h, are shown in Fig. 8. All oxygen contents, z, are less than the maximum value of 3; as the Mn concentration increases, the oxygen content decreases increasingly rapidly.

To investigate possible variation in z two samples, $Nd_{1.00(1)}Mn_{0.95(1)}O_z$ and $Nd_{0.88(1)}Mn_{1.00(1)}O_z$, near each end of the solid solution range, were annealed isothermally in air from 1200 °C to 600 °C in increments of 100 °C for 2 h and quickly cooled. Oxygen contents are shown as a function of temperature in Fig. 9. For both, as the temperature decreases, z increases. Below 700 °C no further changes were observed indicating that the maximum oxygen content obtainable in air at ambient pressure had been achieved. For the Nd-rich composition, z is slightly greater than 3 but for the Mn-rich composition, the maximum z is still significantly less than 3. At any temperature, z for the Mn-rich composition is lower

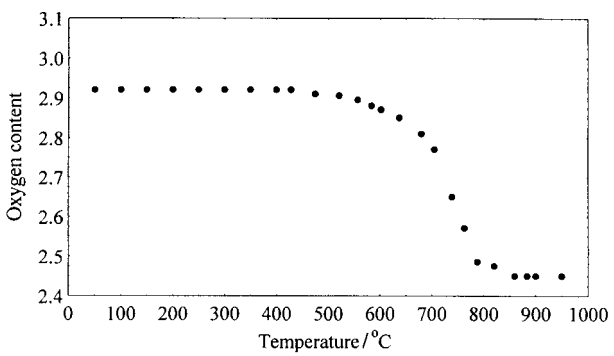

Fig. 7 H_2/N_2 reduction of $Nd_{1.00(1)}Mn_{0.97(1)}O_z$ from which z was calculated to be 2.92(1).

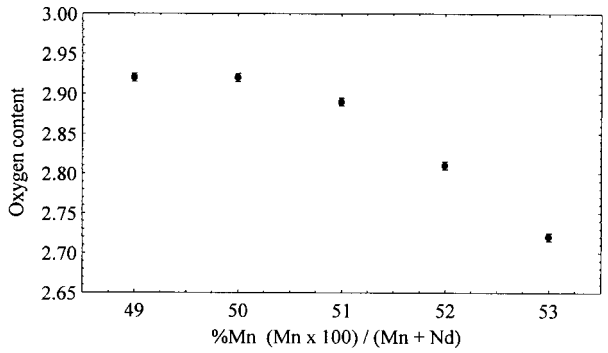

Fig. 8 Variation of the oxygen content with composition of as-fired samples, 1400 °C, 72 h in air.

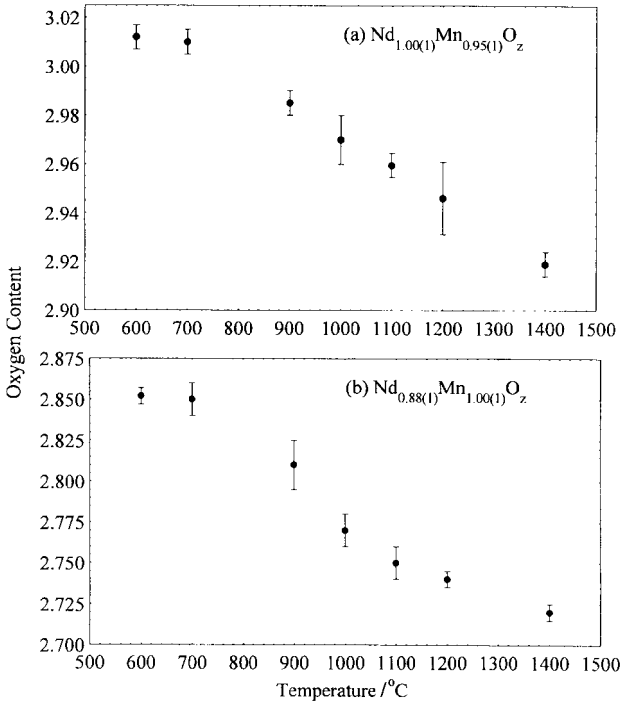

Fig. 9 The oxygen content of $Nd_{1.00(1)}Mn_{0.95(1)}O_z$ and $Nd_{0.88(1)}Mn_{1.00(1)}O_z$ as a function of temperature.

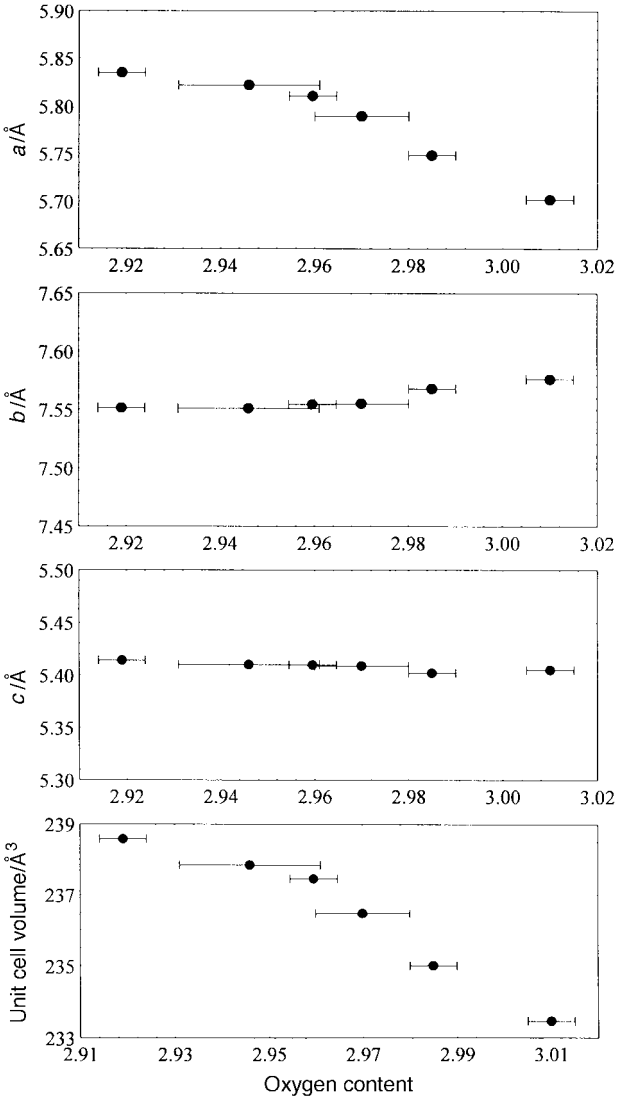

Fig. 10 Variation of the unit cell parameters of $Nd_{1.00(1)}Mn_{0.95(1)}O_z$ with oxygen content.

than that of the Nd-rich composition by ≈0.15–0.20; there is no evidence that samples had reached a constant oxygen content by 1400 °C, the highest temperature studied.

For both compositions, XRD indicated a systematic shift in *d*-spacings with decreasing anneal temperature and hence with increasing *z*. The variation of lattice parameters with *z* is shown in Fig. 10 and 11. As z increases, *a* and *V* decrease, *b* increases and *c* remains roughly constant. Thus the unit cell undergoes an overall reduction in volume and a significant change in shape; it becomes less orthorhombic.

3 Limiting oxygen contents of the 'NdMnO$_z$' solid solution

To try and extend the range of oxygen contents beyond that shown in Fig. 9, samples were heated in both high pressure O_2 and in H_2/N_2. To increase *z*, samples of solid solutions with five different Nd:Mn ratios were annealed at various temperatures under high oxygen pressure (16 h, 200 bar, slow cool 1 °C min^{-1}). After heating at 700 °C, their oxygen contents, *z*, increased (Table 2) indicating that for stoichiometric $NdMnO_z$ and for solid solution samples with a small excess of Mn it is possible to have $z > 3.0$. The unit cell parameters of $Nd_{1.00(1)}Mn_{0.97(1)}O_z$ and $Nd_{0.95(1)}Mn_{1.00(1)}O_z$ (Table 3) change in the same manner as shown in Fig. 10; after high pressure oxygenation, *a* decreases significantly, *b* and *c* increase and *V* decreases. Again the unit cell becomes less orthorhombic with $c \approx a$. The two compositions annealed under high pressure O_2 have different Nd:Mn ratios to those annealed in air. Therefore, their unit cell parameters are not plotted on Fig. 10 and 11 although they show similar trends.

It is not known if the oxygen contents reported in Table 2 are the maximum possible. Certainly high pressure oxygenation is a slow process since samples heated for only 2 h instead of 16 h at 700 °C, 200 bar O_2, showed little evidence of oxygen uptake. Possibly, on heating for longer times at 700 °C or at higher temperatures, *z* values may increase further.

To investigate the lower limit(s) of *z* for the 'NdMnO$_z$' solid solutions, samples were heated by TG in an atmosphere of 10% H_2–90% N_2. Two typical sets of results are shown in Fig. 12. For low Mn contents, samples were stable to reduction up to ≈750 °C and then lost weight rapidly, with complete reduction by 850 °C. Under these conditions it was not possible (but see below) to distinguish between initial reduction of the sample, whilst retaining the original crystal structure, and final decomposition and reduction to MnO and Nd_2O_3.

For higher Mn contents however, reduction commenced at a much lower temperature, ≈500 °C, (Fig. 12), with clear evidence of an intermediate plateau at ≈700 °C before the final weight loss which was complete by 850 °C. XRD patterns for samples reduced only as far as the intermediate plateau

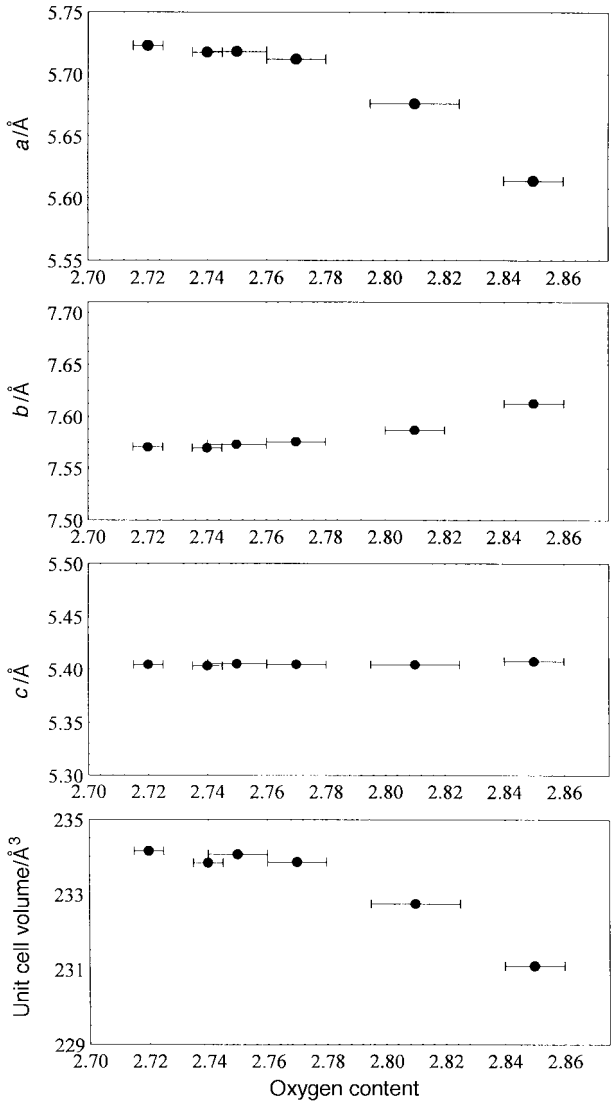

Fig. 11 Variation of the unit cell parameters of $Nd_{0.88(1)}Mn_{1.00(1)}O_z$ with oxygen content.

Table 2 Oxygen content of samples after high oxygen pressure treatment (700 °C, 16 h, 200 bar, slow cool, 1 °C min^{-1})

Sample	Oxygen content
$Nd_{1.00(1)}Mn_{0.97(1)}O_z$	3.00(2)
$Nd_{1.00(1)}Mn_{1.00(1)}O_z$	3.08(2)
$Nd_{0.95(1)}Mn_{1.00(1)}O_z$	3.06(2)
$Nd_{0.91(1)}Mn_{1.00(1)}O_z$	2.98(2)
$Nd_{0.88(1)}Mn_{1.00(1)}O_z$	2.95(2)

Table 3 Oxygen content and unit cell parameters for samples before and after high oxygen pressure treatment

1400 °C for 72 h	700 °C, 16 h, 200 bar, slow cool (1 °C min^{-1})
$Nd_{1.00(1)}Mn_{0.97(1)}O_{2.91(2)}$	$Nd_{1.00(1)}Mn_{0.97(1)}O_{3.00(2)}$
$a=5.8245(19)$ Å	$a=5.5657(22)$ Å
$b=7.5581(20)$ Å	$b=7.6383(33)$ Å
$c=5.4066(17)$ Å	$c=5.4116(28)$ Å
$V=238.01(8)$ Å^3	$V=230.06(14)$ Å^3
$Nd_{0.95(1)}Mn_{1.00(1)}O_{2.89(2)}$	$Nd_{0.95(1)}Mn_{1.00(1)}O_{3.08(2)}$
$a=5.7917(29)$ Å	$a=5.4972(26)$ Å
$b=7.5470(23)$ Å	$b=7.6647(26)$ Å
$c=5.4118(25)$ Å	$c=5.4340(32)$ Å
$V=236.55(11)$ Å^3	$V=228.96(12)$ Å^3

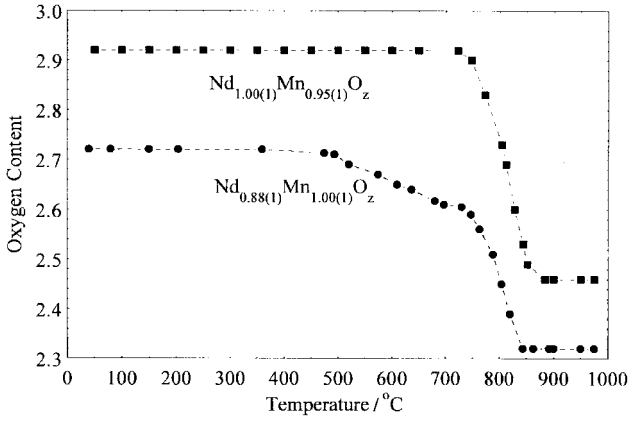

Fig. 12 The H_2/N_2 reduction of $Nd_{1.00(1)}Mn_{0.95(1)}O_z$ and $Nd_{0.88(1)}Mn_{1.00(1)}O_z$.

showed essentially a single phase '$NdMnO_3$' pattern; it appears therefore, that this intermediate plateau represents the lower stability limit for the solid solutions and hence the limiting z values can be obtained from the TG plots. Returning to the TG plot for the Nd-rich sample (Fig. 12), it can be seen that the weight loss has two components with a gradual weight loss below $\approx$800 °C and a more rapid loss above 800 °C. Possibly therefore, the crystal structure of '$NdMnO_z$' is retained during reduction up to $\approx$800 °C but, due to poor resolution, an accurate value for z cannot be estimated. Results are summarised in Table 4 for the limiting z values of the Mn-rich compositions; they show, again, that z decreases with increasing Mn content and also that the oxygen loss occurs more easily (at lower temperatures).

4 Stoichiometry of '$NdMnO_z$': variable Nd : Mn ratios and oxygen content

The stoichiometry range of the $NdMnO_z$ solid solutions is summarised in Fig. 13 in the form of a phase diagram with the oxygen content and cation composition as variables. The cation content is represented both as %cation content for Mn, as earlier, and as variables x and y in the general formula $Nd_{1-x}Mn_{1-y}O_z$. The solid solutions extend to either side of the x=0 and y=0 stoichiometry but are more extensive towards Mn-rich compositions. Oxygen contents are variable for all x and y but gradually decrease with increasing Mn content. Use of the formula $Nd_{1-x}Mn_{1-y}O_z$ with x, $y \geqslant 0$ implies that the maximum Nd, Mn contents in the formula unit are 1.00 and therefore, on departure from the ideal stoichiometry, one or other of the cation sublattices has vacancies. This is discussed later once the crystallographic results have been presented.

For all cation compositions the oxygen contents are variable, depending on the sample heat treatment. For Nd-rich compositions ($y>0$), z can take a small range of values between $\approx$2.9 and 3.0, or slightly greater. For Mn-rich compositions ($x \geqslant 0$), the range of z values increases with x and undergoes a general displacement to lower z values. Thus, with stoichiometric $NdMnO_z$ and with a small Mn excess, maximum oxygen contents can exceed 3.00 and the lower limit of z starts to decrease. By the time the solid solution limit at $x=0.12$ is reached, the oxygen contents cover the range $2.63<z<2.95$.

Table 4 Lower oxygen content limits

Composition	Lower oxygen content
$Nd_{0.98(1)}Mn_{1.00(1)}O_z$	2.83(1)
$Nd_{0.93(1)}Mn_{1.00(1)}O_z$	2.73(1)
$Nd_{0.88(1)}Mn_{1.00(1)}O_z$	2.63(2)

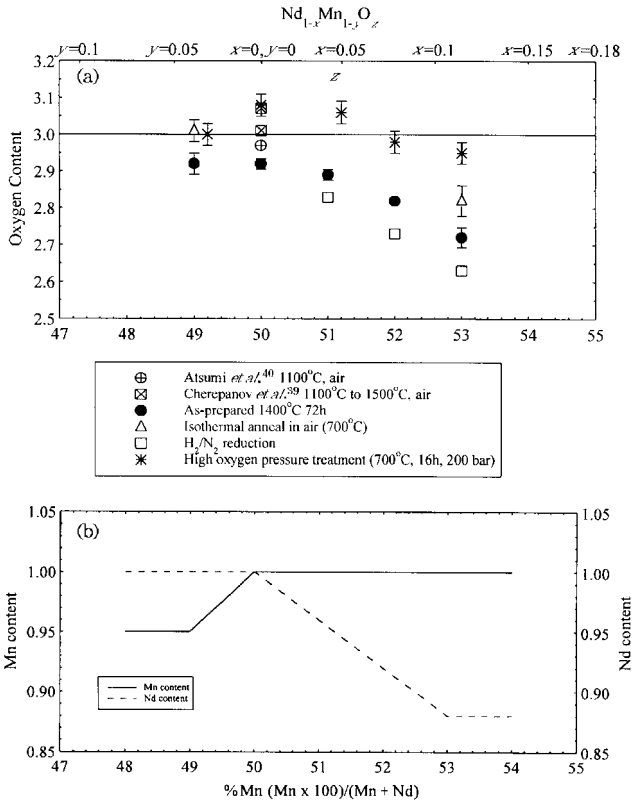

Fig. 13 (a) The oxygen content as a function of Mn concentration. (b) The Mn and Nd content as a function of Mn at% when $z \leqslant 3$.

The oxygen contents determined in this study cover the range reported by Cherepanov *et al.*[39] and Atsumi *et al.*[40] [Fig. 13(a)], although the conditions used to obtain the different z values differed somewhat. Thus, from our results, it is expected that somewhat smaller z values ($\approx$2.9–2.95) would be obtained using the conditions in ref. 39 and 40. Possibly some oxygen uptake occurred during cooling in ref. 39 and 40 whereas our samples were cooled rapidly so as to preserve the high temperature stoichiometry.

5 Neutron diffraction studies

The crystal structure of two compositions near the Nd- and Mn-rich boundaries of the solid solution range were studied: $Nd_{1.00(1)}Mn_{0.97(1)}O_{2.92(2)}$ and $Nd_{0.95(1)}Mn_{1.00(1)}O_{2.83(2)}$. The samples were as-prepared in air so as to have sufficiently large quantities for ND work. Both were refined in space group *Pnma* and, as expected, have the $GdFeO_3$ structure consistent with earlier refinements of these and related rare earth materials. The main objective was to establish the principal defect mechanisms associated with the varying types of nonstoichiometry determined by EPMA and TG analysis.

Atomic coordinates of the $GdFeO_3$ structure were used as initial coordinates for the composition $Nd_{1.00(1)}Mn_{0.97(1)}O_{2.92(2)}$. The Nd site occupancy refined to 1.00(1) and was therefore restrained to unity; Mn and oxygen site occupancies refined below unity (Table 5) with reasonable *R*-factors. The formula deduced from the refinement is $NdMn_{0.96(1)}O_{2.88(2)}$, which is similar to that obtained by EPMA and TG ($Nd_{1.00(1)}Mn_{0.97(1)}O_{2.92(2)}$). It is concluded, therefore, that the average defect structure is described by Mn and O vacancies with full occupancy of the Nd sites. The ND profile is given in Fig. 14(a). Some residual peaks in the difference plot indicate that the refinement was not optimised. Given the large size of the sample and its method of preparation, terminating in an air-cool, it is possible that a small gradient in oxygen content occurred throughout the sample arising from preferential pick-up of oxygen at the sample surface. An improved difference plot might be obtained if the sample is considered as a mixture of two phases having slightly different oxygen contents and therefore slightly different cell dimensions. Such an approach was used successfully to refine the structure of $Sr_{2-x}R_{1+x}Mn_2O_7$, R = La, Nd as a two phase mixture, although the origin of the two phase nature was not clearly established.[22,23] We have not attempted such a refinement here. Whilst a two phase model may give an improved difference plot, this is in part to be expected from the increase in number of refineable parameters that would be used.

Table 5 Structural parameters for $NdMn_{0.97(1)}O_{2.92(2)}$

	Site	*x*	*y*	*z*	*B*	Occ.
Nd	4*c*	−0.0686(2)	0.25	0.0124(2)	0.16(2)	1.00
Mn	4*b*	0.5	0	0	0.006(27)	0.96(1)
O1	4*c*	0.0228(2)	0.25	0.5883(2)	0.18(2)	0.950(8)
O2	8*d*	−0.3188(2)	0.0447(1)	0.2877(2)	0.20(1)	0.968(7)

Cell parameters: 5.87766(4), 7.66068(5), 5.41051(4) Å, R_{wp} = 2.65, R_p = 4.66, X^2 = 11.8561.

Bond lengths and angles for $NdMn_{0.96(1)}O_{2.88(2)}$ are given in Table 6. The Mn–O bond lengths describe MnO_6 octahedra distorted in the 4+2 manner indicative of the static JT effect: Mn–O(2) 1.916(1); Mn–O(2) 2.222(1); Mn–O(1) 1.9518(3) Å. The Nd cation is coordinated by 8 (2.36–2.62 Å)+4 (3.2–3.5 Å) oxygens, as expected for the

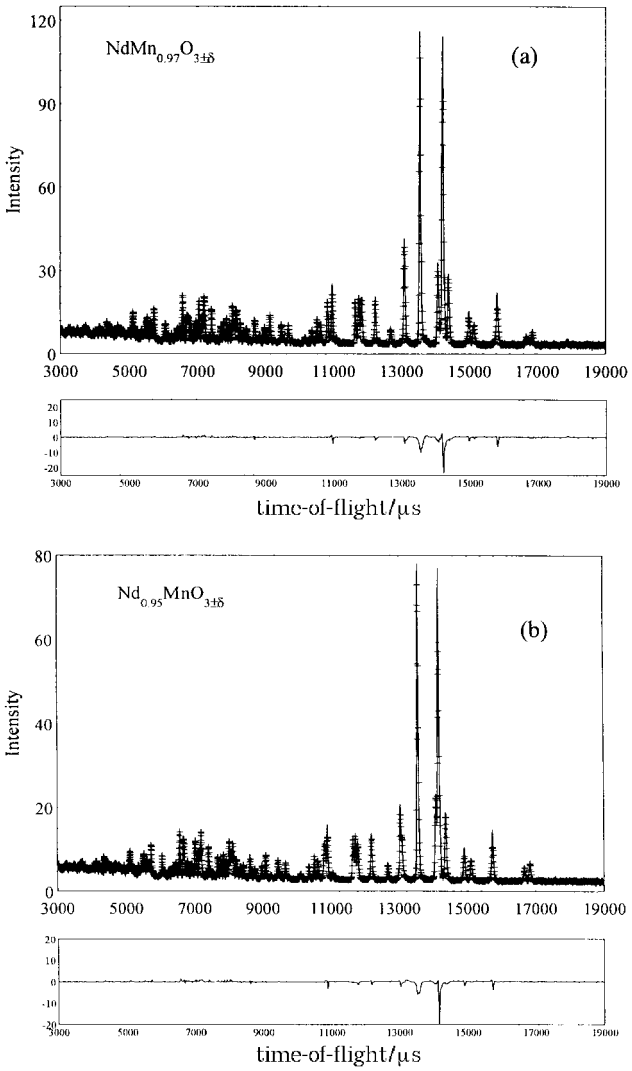

Fig. 14 The observed, calculated and difference neutron diffraction patterns of (a) $NdMn_{0.97}O_{3\pm\delta}$ and (b) $Nd_{0.95}MnO_{3\pm\delta}$.

Table 6 Calculated bond lengths and angles for $NdMn_{0.96(1)}O_{2.88(2)}$

Bond	Bond length/Å	Angle	Bond angle/°
Mn–O2	1.916(1)×2	Mn–O2–Mn	149.44(6)
Mn–O2	2.222(1)×2	O2–Mn–O2	88.78(4)
Mn–O1	1.9518(3)×2	O2–Mn–O2	91.22(4)
Nd–O2	2.393(1)×2	O2–Mn–O1	90.55(4)
Nd–O2	2.620(1)×2	O2–Mn–O1	89.45(4)
Nd–O2	2.604(1)×2	O2–Mn–O1	92.14(4)
Nd–O1	2.357(2)	O2–Mn–O1	87.86(4)
Nd–O1	2.460(2)	O2–Mn–O2	179.98(4)
		O2–Mn–O1	179.98(4)

$GdFeO_3$-type structure. The structure is characterised by co-operative tilting of MnO_6 octahedra arising from a mismatch in ionic radii of Nd and Mn compared with the values expected of A and B cations in the perovskite structure. The corner-sharing MnO_6 octahedra form zig-zag chains parallel to [010] where the top and bottom apices of adjacent octahedra point alternately to and away from the adjacent chains.

For the composition $Nd_{0.95(1)}Mn_{1.00(1)}O_{2.83(2)}$ all thermal parameters and the Nd and Mn site occupancies were first refined. The Mn site occupancy refined to 1.01(1) and was therefore constrained to unity. The thermal parameters were then fixed and the Nd and O occupancies varied (Table 7). The refinement indicated that the Mn content was greater than the Nd content and the oxygen content was less than unity. The formula determined from the refinement, $Nd_{0.98(1)}MnO_{2.92(2)}$, is different in detail from that determined by EPMA and TG, $Nd_{0.95(1)}Mn_{1.00(1)}O_{2.83(2)}$, but clearly indicates Nd, O vacancies as the main defects with fully occupied Mn sites. The different oxygen contents can be attributed to different sample preparation conditions; the sample for EPMA and TG was fired as a pellet which on cooling could take up less oxygen at the sample surface than the powdered sample used for ND. The structure model reported by Pollert *et al.*[46] for $Pr_{0.85}MnO_3$, where the A site is occupied by both the rare earth ion and Mn, was tested but it gave a high R_{wp} value (3.76) and was discounted. The ND profile is given in Fig. 14(b). Again, the difference profile shows residual peaks that may be attributed to inhomogeneity in oxygen content of the sample.

Bond lengths and angles for $Nd_{0.98(1)}MnO_{2.92(2)}$ are given in Table 8. The MnO_6 octahedra are again distorted in the same manner as $NdMn_{0.96(1)}O_{2.88(2)}$ and the structure also is $GdFeO_3$-type with a superposed JT distortion.

Table 7 Structural parameters for $Nd_{0.95(1)}MnO_{2.83(2)}$

	x	*y*	*z*	*B*	Occ.	
Nd	4*c*	−0.0667(2)	0.25	0.0123(3)	0.20	0.984(8)
Mn	4*b*	0.5	0	0	0.07	1.00
O1	4*c*	0.0219(3)	0.25	0.5876(3)	0.20	0.973(9)
O2	8*d*	−0.3176(2)	0.0444(1)	0.2880(2)	0.20	0.971(7)

Cell parameters: 5.78808(4), 7.55640(6), 5.41013(3) Å, $R_{wp}=2.76$, $R_p=3.98$, $X^2=13.4068$.

Table 8 Calculated bond lengths and angles for $Nd_{0.98(1)}MnO_{2.92(2)}$

Bond	Bond length/Å	Angle	Bond angle/°
Mn–O2	1.912(1)×2	Mn–O2–Mn	149.68(6)
Mn–O2	2.192(1)×2	O2–Mn–O2	89.41(4)
Mn–O1	1.9512(4)×2	O2–Mn–O2	90.59(4)
Nd–O2	2.384(1)×2	O2–Mn–O1	90.35(4)
Nd–O2	2.617(1)×2	O2–Mn–O1	89.65(5)
Nd–O2	2.596(2)×2	O2–Mn–O1	92.01(4)
Nd–O1	2.356(2)	O2–Mn–O1	87.99(4)
Nd–O1	2.436(2)	O2–Mn–O2	179.97(4)
		O2–Mn–O1	179.97(4)

Table 9 Calculated bond lengths for $Nd_{0.98(1)}MnO_{3.06(2)}$

Bond	Bond length/Å
Mn–O2	1.905
Mn–O2	2.126
Mn–O1	1.980

Since the Nd, O1 and O2 positions hardly vary between the $Nd_{1.00(1)}Mn_{0.97(1)}O_{2.92(2)}$ and $Nd_{0.98(1)}MnO_{2.92(2)}$ structures, and since Mn occupies the special position 0.5,0,0, it is possible from lattice parameter data to estimate the variation of the JT distortion with changing Mn^{3+} concentration by assuming that the O1 and O2 positions do not change with oxygen content. Comparison of the Mn–O bond lengths (Table 8), for $Nd_{0.98(1)}MnO_{2.92(2)}$, which contains $\approx$100% Mn^{3+} with those calculated for $Nd_{0.98(1)}MnO_{3.06(2)}$, which contains $\approx$80% Mn^{3+} and 20% Mn^{4+} Table 9, suggests a decrease in the Mn–O2 bond lengths as the oxygen content increases, as expected. Further work is required to confirm this.

6 Defect structure and compensation mechanisms

The stoichiometry of the '$NdMnO_3$' solid solution has been characterised by EPMA, TG and ND and expressed, assuming that either the Nd or Mn content can be scaled to one, to give the cation contents per formula unit as a function of composition as shown in Fig. 13. The available evidence indicates that this analysis is valid for all samples where the oxygen content is $\leqslant 3$. For compositions with $z>3$ the description of the stoichiometry has to be reassessed; although we have no direct structural information on these O-rich compositions, oxygen interstitials are not possible within the $GdFeO_3$ structure and the oxygen excess must therefore be accommodated by cation vacancies. Various models are required to describe the stoichiometry of oxygen excess and oxygen-deficient '$NdMnO_3$' which also incorporate the variable Nd : Mn ratio and the variable Mn oxidation state.

First, we present the phase diagram data of Fig. 13(a) again in Fig. 15, but now subdivide the diagram into four quadrants, each with a principal defect structure; each quadrant is separated by lines which also correspond to idealised, simple defect structures. For instance, when $z=3$ the horizontal axis gives

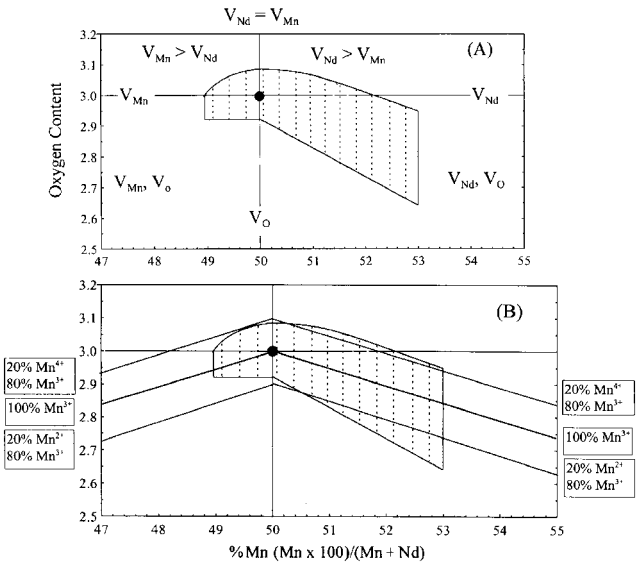

Fig. 15 (A) The phase diagram data of Fig. 13(a), but now subdivided into four quadrants, each with a principal defect structure; each quadrant is separated by lines which correspond to idealised, simple defect structures. Ideal, stoichiometric $NdMnO_3$ is shown as ●. (B) Superposed on the solid solution is the locus of directions with constant Mn oxidation state.

either Nd vacancies ($x>0$) or Mn vacancies ($y>0$). Most of the solid solution compositions lie in the bottom right quadrant with oxygen vacancies and Nd vacancies. Structural data were also obtained for the bottom left quadrant, with oxygen vacancies and Mn vacancies. We have no structural data on oxygen-rich compositions ($z>3$), but given that oxygen interstitials are highly improbable and intergrowth structures with O-rich components have not been found then, for given x and y values cation vacancies must be present within a full oxygen sublattice. For $x>0$, the concentration of Nd vacancies must be greater than that of Mn vacancies and *vice versa* for $y>0$. Fig. 15 demonstrates that, whilst Mn vacancies do occur (in fairly small amounts), the possible concentration of Nd vacancies is much greater. In addition, high Nd vacancy concentrations are favoured by high oxygen vacancy concentrations and *vice versa*.

Thus far we have focused on the defect structure without concern to maintain charge balance. Given that Nd and O always have fixed oxidation states of $+3$ and -2, all stoichiometry variations that cannot be balanced by an ionic mechanism must require an electronic charge balance mechanism involving changes in the Mn oxidation state. In Fig. 15(b), the solid solution is again shown but superposed are the loci of directions with constant Mn oxidation state. A grid is given with the relative amounts of Mn^{2+}/Mn^{3+} and Mn^{3+}/Mn^{4+}, assuming of course that there is no disproportionation in the solid state of Mn^{3+} into mixtures of Mn^{2+} and Mn^{4+}. From this it can be seen that the large majority of the solid solutions are mixed valent with Mn^{2+}/Mn^{3+}; there is also a smaller region of mixed valent Mn^{3+}/Mn^{4+} solid solutions, most of which require high oxygen pressure for their synthesis. Mn-rich samples, synthesised at 1400 °C in air, contain about 20% Mn^{2+} and 80% Mn^{3+}, whereas Nd-rich samples contain mostly Mn^{3+}.

Conclusions

The existence of a small range of '$NdMnO_3$' solid solutions and the appropriate reaction conditions to achieve complete reaction without loss of either component or contamination from the sample container have been established. Solid solutions form where the Nd:Mn ratio can be varied from $Nd_{1.00(1)}Mn_{0.95(1)}O_z$ to $Nd_{0.88(1)}Mn_{1.00(1)}O_z$ and, depending on the thermal history, the oxygen content varies.

Similarly to $RMnO_3$, where R is a rare earth ion from La^{3+} to Dy^{3+}, '$NdMnO_3$' has the orthorhombically distorted $GdFeO_3$ structure with a Jahn–Teller distortion caused by the large proportion of Mn^{3+} ions present. Various defect models describing the stoichiometry and structure of Mn-rich and Nd-rich compositions have been summarised. The defect structure of oxygen-deficient Mn-rich $Nd_{1-x}MnO_z$ compositions involves Nd and O vacancies whereas Mn and O vacancies are present in the Nd-rich $NdMn_{1-y}O_z$ compositions. Further work is required to confirm the 'oxygen excess' defect structures but it is anticipated that they contain both Nd and Mn vacancies within a full oxygen sublattice. There was no evidence of cross-substitution between the A and B cation sites. Stoichiometries deduced by TG, EPMA and ND are in broad agreement. However, homogeneity of oxygen content in large samples prepared for ND may not be complete due to the uptake of oxygen by oxygen-deficient samples on cooling.

Given that $NdMnO_3$ forms over only a limited range of cation stoichiometries, a remarkable range of defect structures is observed involving vacancies on any one or any two of the three sublattices of Nd, Mn and O. Charge compensation is preserved by a mixture of ionic mechanisms, with compensating numbers of cation and anion vacancies and mechanisms in which Mn can adopt any of the three oxidation states $+2$, $+3$ and $+4$. The results are summarised in a novel phase diagram–defect structure map; the range of cation contents corresponds to thermodynamic equilibrium in air at 1400 °C. The range of oxygen contents includes both equilibrium and non-equilibrium conditions since samples were either equilibrated in air at various temperatures or subjected to extremes of oxygen pressure so as to extend the range of oxygen contents into regions where the samples were metastable. Although the cation stoichiometry refers to high temperature equilibrium, it is possible that under different conditions, *e.g.* by low temperature synthesis, a wider range of cation stoichiometry may be accessed.

Acknowledgements

The authors would like to acknowledge the EPSRC for neutron beam time at The Rutherford Appleton Laboratory.

References

1 O. Yamamoto, Y. Takeda, R. Kanno and M. Noda, *Solid State Ionics*, 1987, **22**, 241.
2 Y. Ohno, S. Nagata and H. Sato, *Solid State Ionics*, 1983, **9/10**, 1001.
3 R. van Helmott, J. Wecker, K. Samwer, L. Haupt and K. Bärner, *J. Appl. Phys.*, 1994, **76**, 6925.
4 R. Mahendiran, R. Mahesh, A. K. Raychaudhuri and C. N. R. Rao, *Solid State Commun.*, 1995, **94**, 515.
5 S. Jin, H. M. O'Bryan, T. H. Tiefel, M. McCormack and W. W. Rhodes, *Appl. Phys. Lett.*, 1995, **66**, 382.
6 H. L. Ju, J. Gopalakrishnan, J. L. Peng, Qi Li, G. C. Xiong, T. Venkatesan and R. L. Greene, *Phys. Rev. B*, 1995, **51**, 6143.
7 H. Y. Hwang, S-W. Cheong, P. G. Radaelli, M. Marezio and B. Batlogg, *Phys. Rev. Lett.*, 1995, **75**, 914.
8 F. Damay, A. Maignan, N. Nguyen and B. Raveau, *J. Solid State Chem.*, 1996, **124**, 385.
9 C. Martin, A. Maignan and B. Raveau, *J. Mater. Chem.*, 1996, **6**, 1245.
10 R. Gundakaram, A. Aruvoy, P. V. Vanitha, C. N. R. Rao, N. Gayathri, A. K. Raychaudhuri and A. K. Cheetham, *J. Solid State Chem.*, 1996, **127**, 354.
11 A. Maignan, C. Simon, V. Caignaert and B. Raveau, *J. Appl. Phys.*, 1996, **79**, 7891.
12 R. Mahesh, R. Mahendiran, A. K. Raychaudhuri and C. N. R. Rao, *Mater. Res. Bull.*, 1996, **31**, 897.
13 V. Caignaert, E. Suard, A. Maignan, C. Simon and B. Raveau, *J. Magn. Magn. Mater.*, 1996, **153**, 260.
14 A. J. Millis, B. I. Shraiman and R. Mueller, *Phys. Rev. Lett.*, 1996, **77**, 175.
15 Y. Ng-Lee, F. Sapiña, E. Matrinez-Tamayo, J-V. Folgado, R. Ibañez, D. Beltrán, F. Lloret and A. Segura, *J. Mater. Chem.*, 1997, **7**, 1905.
16 S. Yang, C. T. Lin, K. Rogacki, B. Dabrowski, P. M. Adams and D. M. Speckman, *Chem. Mater.*, 1998, **10**, 1374.
17 J. R. Sun, G. H. Rao and Y. Z. Zhang, *Appl. Phys. Lett.*, 1998, **72**, 3208.
18 A. V. Powell, C. Herwig, D. C. Colgan and A. G. Wittaker, *J. Chem. Mater.*, 1998, **8**, 119.
19 R. A. MohanRam, P. Ganguly and C. N. R. Rao, *J. Solid State Chem.*, 1987, **70**, 82.
20 R. Seshadri, C. Martin, A. Maignan, M. Hervieu, B. Raveau and C. N. R. Rao, *J. Mater. Chem.*, 1996, **6**, 1585.
21 R. Mahesh, R. Mahendiran, A. K. Raychaudhuri and C. N. R. Rao, *J. Solid State Chem.*, 1996, **122**, 448.
22 P. D. Battle, D. E. Cox, M. A. Green, J. E. Millburn, L. E. Spring, P. G. Radaelli, M. J. Rosseinsky and J. F. Vente, *Chem. Mater.*, 1997, **9**, 1042.
23 P. D. Battle, J. A. Hepburn, J. E. Millburn, P. G. Radaelli, M. J. Rosseinsky, L. E. Spring and J. F. Vente, *Chem. Mater.*, 1997, **9**, 3215.
24 P. D. Battle, M. A. Green, N. S. Laskey, N. Kasmir, J. E. Millburn, L. E. Spring, S. P. Sullivan, M. J. Rosseinsky and J. F. Vente, *J. Mater. Chem.*, 1997, **7**(6), 977.
25 R. Seshadri, C. Martin, M. Hervieu and B. Raveau, *Chem. Mater.*, 1997, **9**, 270.
26 R. Seshadri, M. Hervieu, C. Martin, A. Maignan, B. Domenges and B. Raveau, *Chem. Mater.*, 1997, **9**, 1778.
27 R. S. Liu, L. Y. Jang, J. M. Chen, J. B. Wu, R. G. Liu, J. G. Lin and C. Y. Huang, *Solid State Commun.*, 1998, **105**(9), 605.
28 Y. Shimakawa, Y. Kubo and T. Manako, *Nature*, 1996, **379**, 53.

29 B. C. Tofield and W. R. Scott, *J. Solid State Chem.*, 1974, **10**, 183.
30 N. Sakai, H. Fjellvåg, B. Lebech and M. T. Fernandez-Diaz, *Acta Chem. Scand.*, 1997, **51**, 904.
31 A. Maignan, C. Michel, M. Hervieu and B. Raveau, *Solid State Commun.*, 1997, **104**(4), 277.
32 S. Geller, *J. Chem. Phys.*, 1956, **24**, 1236.
33 J. A. M. van Roosmalen, E. H. P. Cordfunke, R. B. Helmholdt and H. W. Zandgergen, *J. Solid State Chem.*, 1994, **110**, 100.
34 J. Töpfer, J-P. Doumerc and J-C. Grenier, *J. Mater. Chem.*, 1996, **6**, 1511.
35 J. Töpfer, *Chem. Mater.*, 1997, **9**, 1476.
36 J. Töpfer, *J. Solid State Chem.*, 1997, **130**, 117.
37 J. A. Alonso, M. J. Martinez-Lope, M. T. Casais, J. L. MacManus-Driscoll, P. S. I. P. N. de Silva, L. F. Cohen and M. T. Fernandez-Diaz, *J. Mater. Chem.*, 1997, **7**, 2139.
38 J. A. Alonso, M. J. Martinez-Lope and M. J. Casais, *Eur. J. Solid State Inorg. Chem.*, 1996, **33**, 331.
39 V. A. Cherepanov, L. Yu. Barkhatova, A. N. Petrov and V. I. Voronin, *J. Solid State Chem.*, 1995, **118**, 53.
40 T. Atsumi, T. Ohgushi, H. Namikata and N. Kamegashira, *J. Alloys Compd.*, 1997, **252**, 67.
41 R. I. Smith and S. Hull, Report RAL-TR-97-038, Rutherford Appleton Laboratory, Oxon, UK, 1997.
42 W. I. F. David, R. M. Ibberson and J. C. Mathewsan, Report RAL-92-032, Rutherford Appleton Laboratory, Oxon, UK, 1992.
43 V. F. Sears, *Neutron News*, 1992, **3**, 26.
44 JCPDS, International Centre for Diffraction Data, Newton Square, Pennsylvania, 19073-3273, USA.
45 J. B. Goodenough, *Magnetism and the Chemical Bond*, John Wiley and Sons, New York, 1963.
46 E. Pollert and Z. Jirák, *J. Solid State Chem.*, 1980, **35**, 262.

Paper 9/00734B